

## CRISS-CROSS MAPPING OF BD+30 3639: A NEW KINEMATIC ANALYSIS TECHNIQUE

WOLFGANG STEFFEN<sup>1</sup> AND NICO KONING<sup>2</sup>

<sup>1</sup> Instituto de Astronomía, Universidad Nacional Autónoma de México, C.P. 22860, Ensenada, Mexico; [wsteffen@astroen.unam.mx](mailto:wsteffen@astroen.unam.mx)

<sup>2</sup> Department of Physics and Astronomy, University of Calgary, SB 605, 2500 University Drive NW, Calgary, AB T2N 1N4, Canada; [nkoning@iras.ucalgary.ca](mailto:nkoning@iras.ucalgary.ca)  
Received 2010 September 25; accepted 2010 December 15; published 2011 February 1

### ABSTRACT

We introduce a new method to analyze kinematic proper motion data. The method is called “criss-cross” mapping. It emphasizes regions where proper motion vector extensions cross or converge. From a superposition of lines through the vectors a map is generated which helps to interpret the kinematic data. The new mapping technique is applied to the young planetary nebula BD+30 3639. The data are more than 200 internal proper motion measurements from Li et al. From the criss-cross mapping of BD+30 3639, we conclude that the kinematic center is approximately 0.5 arcsec off-set to the southeast from the central star. The mapping also shows evidence for a non-homologous expansion of the nebula that is consistent with a disturbance due to the bipolar molecular bullets.

*Key words:* ISM: kinematics and dynamics – methods: data analysis – planetary nebulae: individual (BD+30 3639)

*Online-only material:* color figures

### 1. INTRODUCTION

The complex structure found for many (proto-) planetary nebulae (PNe) has introduced considerable problems into the theory of their formation processes. Spatially resolved spectroscopy has shown that objects which have apparently spherically symmetric images may be more complex along the line of sight. For example, bipolar nebulae seen along the line of sight mimic spherical or elliptical ones. An example that has often been discussed as being either ellipsoidal or bipolar is the Ring Nebula (M57) (e.g., Bryce et al. 1994; Guerrero et al. 1997; Steffen et al. 2007). High-quality reconstructions of the three-dimensional (3D) structure of PNe are therefore an essential ingredient to find the formation mechanisms and the nature of the central objects. Knowledge of the 3D structure of as many nebulae as possible can help resolve the debate over the role of single versus multiple central stars in the structure formation (Balick & Frank 2002). Furthermore, accurate 3D models of the expanding nebulae can improve the distance determination from angular expansion measurements (Li et al. 2002, hereafter LHB2002). Caveats for the distance determination from expansion parallaxes have been discussed by Mellema (2004) and Schönberner et al. (2005).

Knowledge of the 3D structure of PNe is a fundamental ingredient for the development of a consistent theory for individual objects and the overall class of PNe. Since the two-dimensional (2D) projected image does not provide the full 3D structure information, additional constraints have to be obtained for the reconstruction. For expanding objects like PNe kinematic information may produce sufficient constraints if a few reasonable assumptions can be made. A common assumption is that the expansion is radial from the central star and the magnitude of the velocity is proportional to distance, i.e., the velocity vector is proportional to the position vector (homologous expansion). This allows a direct mapping of the radial velocity component to the position along the line of sight, if the constant of proportionality can be determined otherwise. In this case, some degree of symmetry of the whole or part of the object is sufficient to generate a unique mapping.

Hydrodynamic calculations and numerical simulations based on the generalized interacting stellar wind model show that the expansion of shell-like PNe with active winds should be non-homologous (Steffen et al. 2009, and references therein). In the velocity field, a nonlinear variation of the velocity magnitude and measurable deviations from the radial direction are expected.

Very clumpy PNe may develop an approximately homologous expansion due to the differential acceleration of different density components of the ambient medium into which the fast stellar wind expands (Steffen & López 2004). In this model, the density dependence of the terminal velocity of a clump can lead to a considerable spread in the velocity for a given distance from the central star. This makes a unique mapping from velocity to position correspondingly uncertain.

Additional kinematic information can be obtained from proper motion measurements of internal features. Such measurement can potentially reveal the non-radial expansion of a nebula. This information can then be taken into account during 3D reconstruction to correct inaccuracies introduced by assuming homologous expansion (Steffen et al. 2009).

The high spatial resolution and the extended lifetime of the *Hubble Space Telescope* (HST) have allowed the observation of expanding nebulae with a time span of the order of 15 years. To date, this has been sufficient to measure the angular expansion of only a few PNe with sharp features like clumps or thin shells (e.g., O’Dell et al. 2009; Meaburn et al. 2008).

BD+30 3639 is a young PN that has been observed in detail with a variety of observational techniques. It shows extended emission from radio to X-rays. The structure is, however, substantially different in the various wavelength regions. Figure 1 is a composite image that shows images taken in the different wavelength regions within a single frame. Some of the most striking features are as follows. First, the basic projected structure is a nearly rectangular ring, with some emission inside. The ring is not uniform along its perimeter, but shows reduced brightness in some directions, especially in the southwestern region. Second, a fainter halo has been observed to go out to at least twice the distance of the ring (Harrington et al. 1997). The infrared continuum emission roughly traces the optical

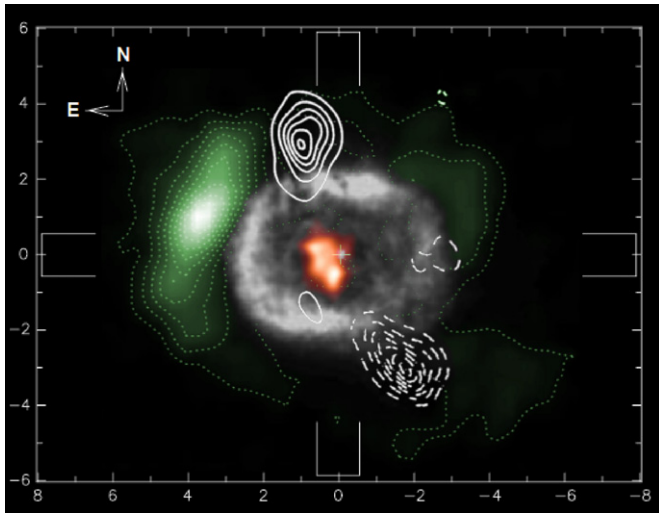


**Figure 1.** Several types of maps combined: optical (gray, from LHB2002), H<sub>2</sub> (green contour, from Shupe et al. 1998), CO (white contour, from Bachiller et al. 2000), and the criss-cross map (red, this work).

(A color version of this figure is available in the online journal.)

rectangle and its halo. Third, molecular hydrogen emission is distributed very unevenly in large clumps within the halo (Shupe et al. 1998). The molecular CO lines show a pair of high-speed bullets moving in opposite directions (Bachiller et al. 2000). Finally, extended X-ray emission has been observed inside the optical rectangle with a brightness gradient going roughly from southwest to northeast (Kastner et al. 2000).

Proper motion combined with Doppler-velocity measurements and an accurate 3D model of the object may help improve the distance determination of the object. LHB2002 have used two *HST* narrowband images that were observed with a separation of 5.663 years. They determined the expansion of the nebula along many angular sectors as well as local proper motion vectors of substructure at nearly 200 positions. With their measurements and an ellipsoidal model of BD+30 3639 they determined a distance of 1.2 kpc.

One of their results is that the expansion seems to be somewhat faster along position angles (P.A.s) around 40° and 220°. This coincides approximately with the P.A.s of the CO outflows (Figure 1). LHB2002 concentrate on the variation of the magnitude of the proper motion vectors as a function of P.A. and distance from the central star.

In this paper, we analyze their proper motion vectors with emphasis on the direction, i.e., their deviation from the radial direction, as a function of P.A. and distance from the central star (Figure 2). The deviation shows systematic variations around the flat distribution expected from a homologous expansion. Extending the velocity vectors over the full area of the object has led us to develop a new method of analyzing internal proper motion data: “criss-cross mapping.”

The layout of our paper is as follows. We first describe the new criss-cross mapping in general terms in Section 2. In Section 3, we show examples of theoretically relevant criss-cross maps as well as the changes introduced by structure, sampling or errors in the observations. Finally, in Sections 4 and 5 we describe and discuss our results for BD+30 3639, respectively.

## 2. CRISS-CROSS MAPPING

In order to help in the interpretation of current and future internal proper motion measurements in expanding nebulae,

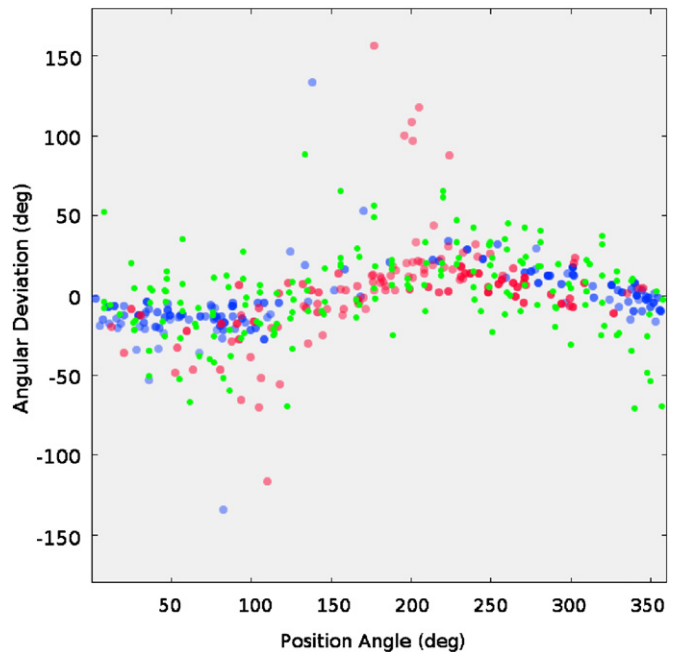


**Figure 2.** Angular deviation from the radial direction of the internal proper motion vectors plotted against position angle. Data extracted from LHB2002 are in green and model values from this work are in red and blue.

(A color version of this figure is available in the online journal.)

we introduce “criss-cross mapping.” The purpose is to detect and emphasize regions where velocity vectors converge and intersect. A radially expanding nebula will have all its velocity vectors intersect at the position of the central star. If there are systematic deviations from radial expansion, the intersection point might shift or be transformed into some extended pattern. Such a pattern reveals helpful information. The criss-cross mapping procedure is related to the concept of optical caustics, where reflected or refracted light rays may define a line or surface to which they are all tangent and adjacent rays cross.

We define the criss-cross mapping in its most basic form by the following procedure, which is then cast in mathematical form.

We replace every proper motion vector with a thin line that extends over the complete area covered by the nebula. We assign a finite constant brightness to every such line, and generate an image by adding together all lines. Finally, the result is convolved with a suitable kernel, for instance, a Gaussian with a width that is larger than the average separation between the vectors. In the regions where vectors converge, the resulting image will increase in brightness and prominently reveal where most velocity vectors meet. Let us first consider the theoretical case of a continuous velocity vector field  $\vec{v}(x, y)$  projected on the plane of the sky in Cartesian coordinates  $(x, y)$ . An actual observation will, of course, have only a sample of  $N$  vectors over a limited field of view. This case will be treated below.

For a simple mathematical formulation of criss-cross mapping, for every velocity vector we add a thin line through it that extends over the whole image plane. Such a line can be described as a Dirac delta distribution  $\delta(d)$  perpendicular to it with a constant weight number  $w$  (Figure 3, left). All the added vector lines together constitute the raw criss-cross map. The weight  $w$  of each line can be related to the error in the measurement of the velocity vector, the velocity magnitude, or some other

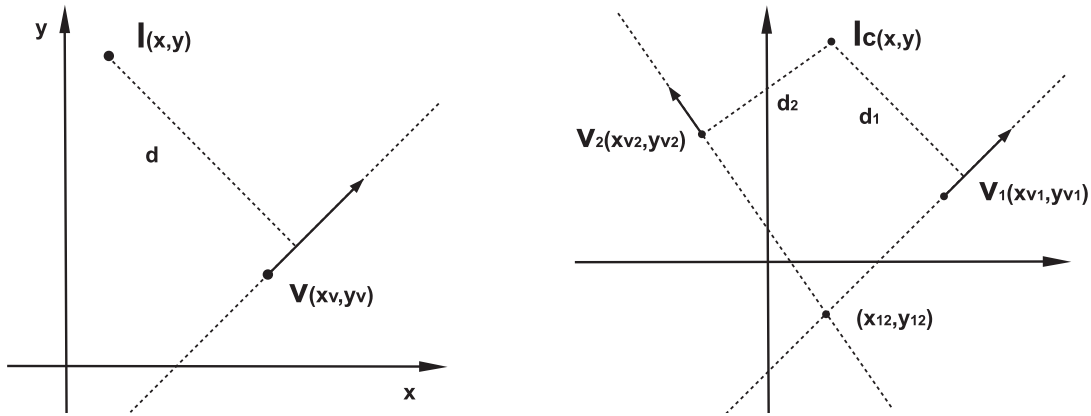


**Figure 3.** Geometrical elements for the two criss-cross mapping procedures,  $I$  and  $I_c$ , on the left and right, respectively. For  $I$ , a single vector line defined by the velocity vector  $V(x, y)$  has a distance  $d$  to the mapping position  $(x, y)$ . For  $I_c$  the distances from two vector lines are used to determine whether the mapping point  $(x, y)$  is in the crossing region (hence the subscript  $c$ ) of the vector lines around  $(x_{12}, y_{12})$ .

quantity that might provide additional information to the map. Before convolution with a kernel, the raw map intensity  $I(x, y)$  is then given by

$$I(x, y) = \iint w_{(x_v, y_v)} \delta(d(x, y; x_v, y_v)) dx_v dy_v. \quad (1)$$

The distance  $d(x, y; x_v, y_v)$  from a point  $(x, y)$  to the line through a vector  $\vec{v}(x_v, y_v)$  can be expressed as

$$d(x, y; x_v, y_v) = \left| \frac{v_{xv}}{v} (y_v - y) - \frac{v_{yv}}{v} (x_v - x) \right|, \quad (2)$$

where  $v_{xv}$  and  $v_{yv}$  are the components of the velocity vector. The mapping prescription above takes into account and adds together the full lines.

A more restricted version is to consider only the crossing points of the lines. Then the points can be selected using two Dirac delta distributions (Figure 3, right) with a raw point map  $I_c(x, y)$  given by

$$I_c(x, y) = \iiint w_{1(x_{v1}, y_{v1})} \delta(d(x, y; x_{v1}, y_{v1})) \times w_{2(x_{v2}, y_{v2})} \delta(d(x, y; x_{v2}, y_{v2})) dx_{v1} dy_{v1} dx_{v2} dy_{v2}. \quad (3)$$

The final map  $I_f(x, y)$  is then obtained by convolution of  $I(x, y)$ , or  $I_c(x, y)$ , with a suitable smoothing kernel  $\kappa(u, v)$ :

$$I_f(x, y) = \iint I(x - u, y - v) \kappa(u, v) du dv. \quad (4)$$

### 2.1. Basic Analytic Examples

We will now discuss theoretical criss-cross maps for two continuous velocity vector fields that produce point-like  $I_c$  maps: radial expansion and radial expansion with a constant additive component.

For the radial expansion, the criss-cross vectors are obviously expected to meet at the center. This can be shown using Equation (2). Without loss of generality, consider the two-dimensional case in the  $(x, y)$ -plane for a 3D configuration that is cylindrically symmetric around the  $z$ -coordinate. Take two vectors at positions  $(x_1, y_1)$  and  $(x_2, y_2)$ . The homologous velocity field is given by  $\vec{v} = k\vec{r}$ , where  $k$  is a constant and  $\vec{r}$  is the position vector  $(x, y)$ . We look for the position  $(x, y)$  where the two lines through the velocity vectors at  $(x_1, y_1)$  and

$(x_2, y_2)$  meet. This is the position where the distance given by Equation (2) vanishes for both vectors, i.e.,  $d_1 = d_2 = 0$ . Inserting the homologous velocity law leads to

$$\frac{x}{y} = \frac{x_1}{y_1} = \frac{x_2}{y_2}. \quad (5)$$

The only solutions are identical lines along the same radial direction, i.e., lines with the same slope, or non-parallel lines that meet at the origin  $(x, y) = (0, 0)$ . Since the positions of the vectors  $(x_1, y_1)$  and  $(x_2, y_2)$  have not been restricted, the solution is true for all vectors. This is, of course, the expected result. This solution corresponds to the single point of non-zero emission in the raw point map from Equation (3).

For a homologous expansion  $\vec{v} = k\vec{r}$  plus a constant component, we consider a constant component along the  $z$ -axis,  $v_z = v_c$ . A similar calculation to the one above shows that again there is a single crossing point, but now at the position  $(v_c/k, 0)$ . If the cylindrical distribution is bipolar, i.e.,  $v_z = v_c$  for  $z > 0$  and  $v_z = -v_c$  for  $z < 0$ , then there will be two convergence points on the symmetry axis at  $(v_c/k, 0)$  and  $(-v_c/k, 0)$ , respectively.

The criss-cross maps of more complex velocity fields can be considered as the composition of elemental fields that produce such point-like maps. Any spatial distribution can be divided into regions of vectors that meet at a single point. The trivial and worst case would be regions of only two vectors. For example, the case of a homologous field plus a linearly increasing magnitude can be considered as a field with sectors of cylindrical components that depend on the position along the axis,  $v_c(z) = gz$ , where  $g$  is a constant. The meeting point of the vector lines is therefore spread along the axis. In this case, there are two crossing points that are off-axis leading to ‘‘side-lobe’’ structures (see Section 3).

In the following sections, we discuss and apply the numerical implementation of the full line mapping of Equation (1) and show criss-cross maps of a few basic velocity fields, including that of a homologous expansion with a bipolar component that increases linearly with distance along the axis to reveal the off-axis components.

### 2.2. Numerical Implementation

In practice, the number of integrals involved in the criss-cross mapping process makes the calculation of a continuous

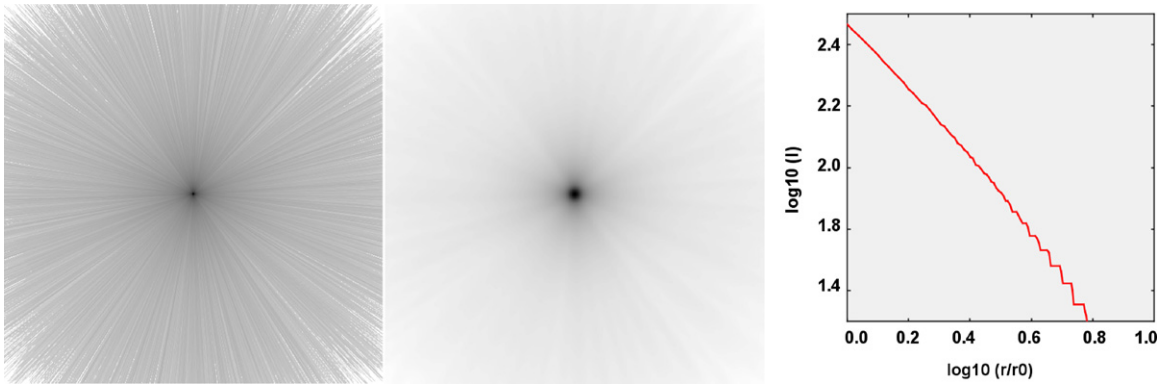


**Figure 4.** Fundamental criss-cross map for a radially expanding sphere with 20,000 vectors that have been randomly distributed in the sphere. On the left is the full resolution version where every line has a thickness of 1 pixel (image size is  $256 \times 256$  pixels). This image has been convolved with a Gaussian kernel of 14 pixel FWHM (middle image). On the right is the log–log brightness profile along a slit starting at the center of the smoothed criss-cross map. The slit has a constant width similar to the width of the Gaussian kernel (the brightness is normalized to 255). The step structure at large distances is due to the limited dynamical range of the image.

(A color version of this figure is available in the online journal.)

vector field very time consuming. Fortunately, in terms of computing effort, the number of vectors available in a real set of observations is rather small, at best a few hundred. For the case of BD+30 3639, as measured by LHB2002, there are approximately 200 vectors available. Our numerical scheme determines whether an image pixel  $(i, j)$  is on a line going through the vector indexed  $k$ . If so, then the weight value  $w_k$  is added to the pixel. We use a discrete version of Equation (1) in the following form:

$$I_{d,i,j} = \sum_{k=1}^{n_k} w_k \delta(d_{i,j}; k, s), \quad (6)$$

where  $i, j$  are the indices of the image pixels,  $k$  is the velocity vector index, and the total number of velocity vectors is  $n_k$ . The distance of the image pixel  $i, j$  to the vector line  $k$  is  $d_{i,j}$ . In Equation (6),  $\delta(d)$  is a top-hat function with a value of 0 or 1. The total width of the top-hat function—which represents the line width—is  $s$ . In practice,  $\delta(d)$  can also be some other smoother function than a step function, including a Gaussian.

We have implemented this simple procedure in the morphokinematic 3D modeling software *Shape* (Steffen et al. 2011; *Shape* is available from <http://www.astrosen.unam.mx/shape>). It allows one to generate criss-cross maps from observations and models. In our implementation, the weight  $w_k = 1/n_k$  normalizes the raw image to the maximum value obtained for a radially expanding velocity field, i.e., when all vector lines merge at a single point. The resulting raw image is then convolved with a Gaussian kernel. The final image can then be normalized to a suitable value for the output device and further processed, e.g., with an appropriate lookup table to emphasize the features of the map.

### 3. EXAMPLES OF CRISS-CROSS MAPS

We now discuss a few basic examples that illustrate some of the general properties of criss-cross mapping.

#### 3.1. Deviations from Homologous Expansion

Our primary scientific goal in this research is to establish whether there are non-radial deviations from a homologous

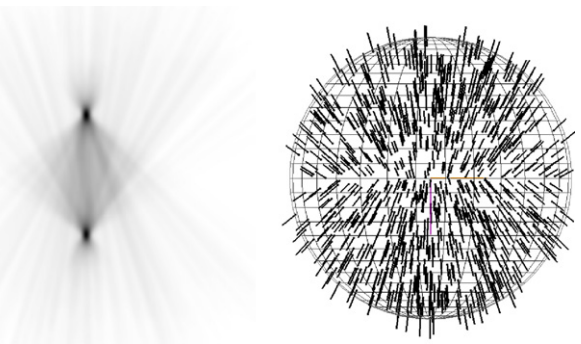


**Figure 5.** Criss-cross map for a homologous + constant bipolar velocity field. It shows the characteristic double peak at each side of the center. As shown on the right, for this map we have used 1000 randomly distributed velocity vectors in a spherical volume.

(A color version of this figure is available in the online journal.)

expansion in a PN. Therefore we take the criss-cross map of a homologously expanding and uniformly filled sphere as a reference. Figure 4 shows the criss-cross map for this case. We used 20,000 individual vectors in order to obtain a quasi-continuous distribution (Figure 4, left and middle). A plot of the brightness profile of the smoothed map is also shown (Figure 4, right). Such brightness profiles might produce useful additional information if sufficient velocity vectors are available. As expected, the criss-cross lines converge at the center and produce a single peak. The first examples in this section are all oriented with the symmetry axis perpendicular to the line of sight and in the vertical direction. Examples of deviations from this orientation will also be discussed below.

As discussed in Section 2.1, adding a constant velocity component to the homologous field will shift the peak position and an added bipolar cylindrical component will produce a double peak in opposite directions. Figure 5 shows the 3D vector field and criss-cross maps of this case, confirming the double peak structure. A secondary crossing pattern, or “side lobes,” is also apparent.

When the cylindrical component increases linearly with distance along the axis, the bright region of the criss-cross map is smeared out into a linear feature, since the  $v_c/k$  is now a function of  $z$  (Figure 6, left). Side lobes have a caustic-like

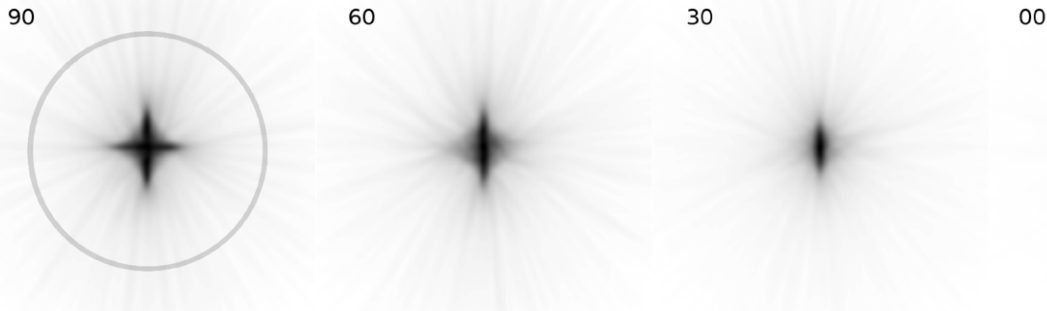


**Figure 6.** Criss-cross maps for a filled sphere with a velocity field of homologous expansion plus a component that increases linearly along the  $z$ -axis ( $0 < v_c(z)/k < 0.5$ ). The circle marks the outer radius of the sphere. The inclination of the symmetry angle with respect to the line of sight changes from  $90^\circ$  to  $0^\circ$  from left to right, respectively.

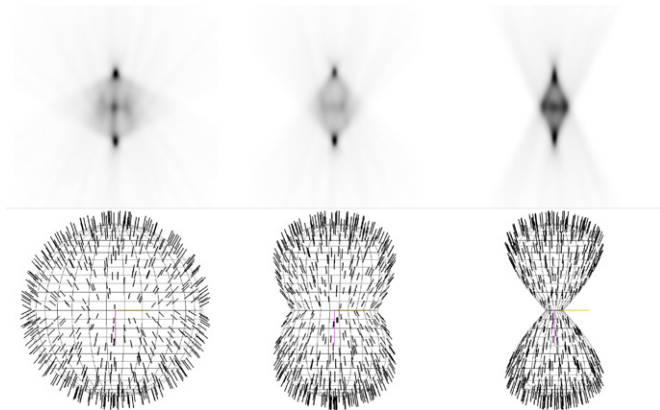


**Figure 7.** Criss-cross maps for different degrees of bipolarity but the same velocity field (radial expansion with a bipolar constant component along the vertical axis in the image). The primary structure of the map remains the same for all with the peaks at the same positions. However, the secondary structure changes with the distribution of velocity vectors.

(A color version of this figure is available in the online journal.)

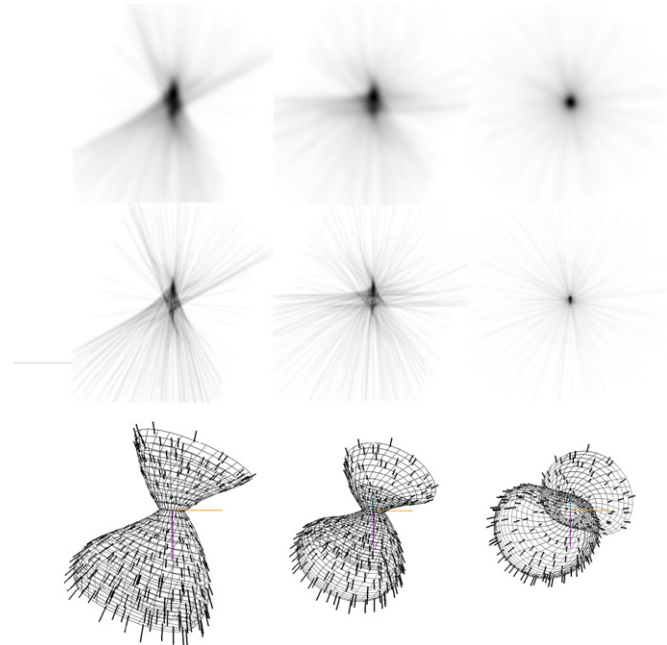
structure, the size of which is determined by the maximum of  $v_c(z)/k$  as described in Section 2.1.

Figure 6 shows how the cross pattern changes with inclination angle of the object. The bright horizontal section of the cross becomes diffuse and at high inclination angles disappears. The side lobes become very diffuse. The length of the axial bright line becomes smaller as the projection of the cylindrical component on the image plane shrinks. When the object is viewed along the axis, the cylindrical component vanishes and the criss-cross map is point like.

### 3.2. Effects of Sampling and Object Structure

The quality of a criss-cross map will vary with the number, distribution, and precision of the proper motion measurements within an object. Careful consideration of the effects of sampling and measuring errors has to be made in order not to overinterpret the derived criss-cross map. In this section, we show how the mapping changes with the number of sampling points and measuring errors.

Figure 7 shows how a change from spherical to bipolar structure with a fixed velocity field affects the criss-cross mapping. The primary structure and position of a bright double peak is conserved, but the side lobes change considerably. Also the brightness ratio between the primary peaks and the side lobes changes with the distribution of the velocity vectors. The reason is that the number of vectors passing through the main



**Figure 8.** Criss-cross maps for a distorted and partial bipolar nebula with a homologous + linearly increasing bipolar component along the axis. The object is seen at three different inclination angles ( $0^\circ$ ,  $45^\circ$ , and  $80^\circ$ , left to right, respectively). Maps with two different Gaussian convolution kernels are displayed to show the influence of the resolution. Note that at  $80^\circ$  inclination the double peak in the map can still be distinguished at the higher resolution.

(A color version of this figure is available in the online journal.)

peaks is practically the same, while the secondary crossings are spread out over a larger area in the spherical than in the bipolar distribution.

The behavior with changing viewing angle for a non-spherical structure and velocity field can be followed in Figure 8. For two different smoothing kernels (top and middle), the structure rotates with its axis from perpendicular to the line of sight (left) to near alignment with the viewing direction (right). The non-homologous nature of this cylindrically symmetric velocity field can be better appreciated with a larger angle between the axis and the line of sight. When the object is nearly aligned with the viewing direction, the non-homologous nature of the velocity field can only be derived with higher resolution, i.e., a small smoothing kernel. It is important to choose an adequate kernel for a particular purpose, since large kernels reduce noise, but high resolution may be necessary to identify small features that can very well be real.

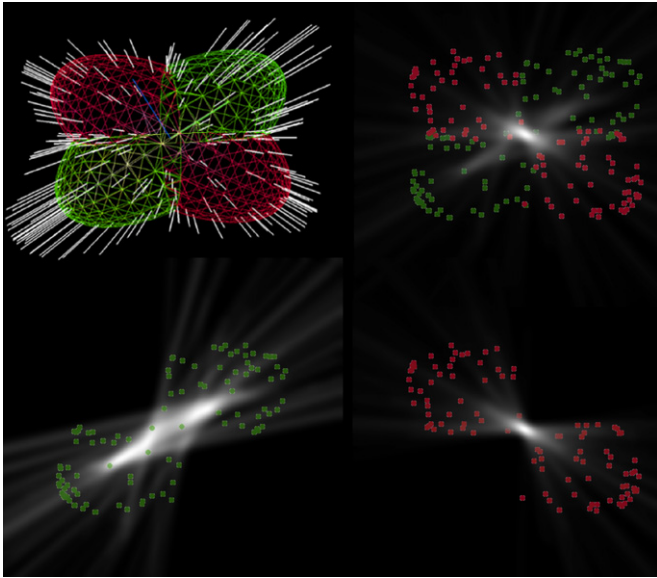


**Figure 9.** Simple model of a multi-polar nebula. A main ellipsoidal section (red) has been deformed by an oblique bipolar outflow (green). Along its axis the bipolar outflow adds a linearly increasing velocity component to the overall homologous expansion. The top left shows the projected velocity vectors used to produce the criss-cross map in the other images. The positions of the vectors are superimposed on the map. One hundred vectors were used for each region. In the criss-cross maps their positions are marked with colored dots.

(A color version of this figure is available in the online journal.)

Some objects might have regions that disturb an otherwise homogeneously expanding object. To test whether this effect can be detected with criss-cross maps, we made a multi-polar model with an overall homologous expansion. However, two opposite bumps have an additional increasing velocity component along their axes (Figure 9). If the disturbance is sufficiently large, the criss-cross map reveals which of the bumps has the non-homologous velocity component by showing a linear extension in their direction (Figure 9, top right). In the projection drawn in Figure 9, the four bump regions are spatially distinct and can be analyzed separately. The separated bumps are shown in the lower part of the same figure where the difference in the velocity field can be clearly appreciated from the individual criss-cross maps.

When the viewing angle is not as favorable, the two regions can be superimposed in projection. In that case, criss-cross mapping may still reveal the presence of a non-homologous velocity component. Figure 10 shows the vectors (top) and the criss-cross map for the same object as the previous multi-polar case, but seen from a different viewing angle. The disturbing bipolar ejection can still be detected as an extended linear feature.

An important observational problem is the number of sampling points from which the transverse velocity can be reliably determined. The number of sampling points that can be obtained depends strongly on the object structure. Smooth distributions are very difficult and highly structured objects with many localized small-scale brightness maxima are best suited. In Figure 11, we show how a criss-cross map may change with the number of available sampling points, between 2000 and 50 vectors. It is found that the key structure of the map does not change very much and the double peak nature of the criss-cross map is almost as clear in the case of 50 as in that of 2000 vectors. This shows that the number of vectors can be quite modest and still

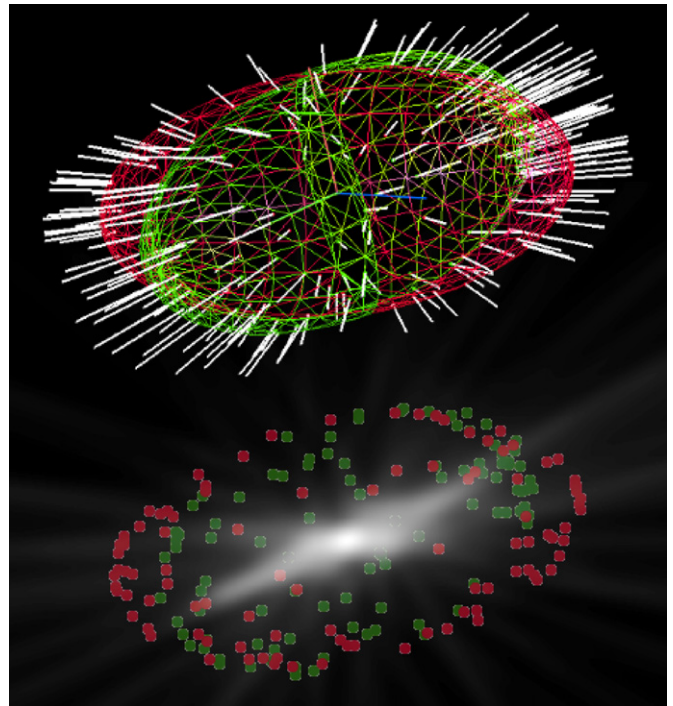


**Figure 10.** Same model as the one from Figure 9 but from a different viewing angle where the bipolar outflow is projected in the same area as the main nebula and cannot be separated spatially. If features from each section can be identified to separate their velocity vectors, the presence of the non-homologous bipolar outflow can be detected as such from the criss-cross map.

(A color version of this figure is available in the online journal.)

yield clear information that is very helpful in the interpretation of the velocity field.

The distribution of velocity vectors that can be measured on an object is strongly dependent on the distribution of brightness. In smooth low brightness regions, the proper motion measurements will be much more difficult if possible at all, compared to regions with high-contrast bright and knotty structures. Within the regions that allow proper motion measurements, the distribution of proper motion vectors that can be measured on an object is likely to be irregular. Therefore, in Figure 12 we study how the random distribution of the sampling positions can modify the criss-cross map. In this model, the exact position of a vector is random, with a uniform average distribution per area of the nebula shell. Each map has the same 3D velocity field and structure. The difference is only in the individual position of the 200 or 50 vectors on the object (left and right, respectively).

For a test object with 200 vectors the overall structure of the criss-cross map is quite consistent, with significant changes only in the relative brightness of the main peaks and minor changes in the secondary structure. The differences are more pronounced for the case of 50 vectors, but the overall pattern is still clearly recognizable.

Finally, in Figure 13 we study how a random velocity component on a fixed background alters the maps. Such a random component could physically be caused by turbulent motion or by measuring errors for the proper motion vectors. In our test example, we have increased the random component from map to map. Until the random component becomes comparable to the systematic velocity field, the overall disturbance to the maps is rather small and still allows clear conclusions. However, when the random component becomes similar to the systematic

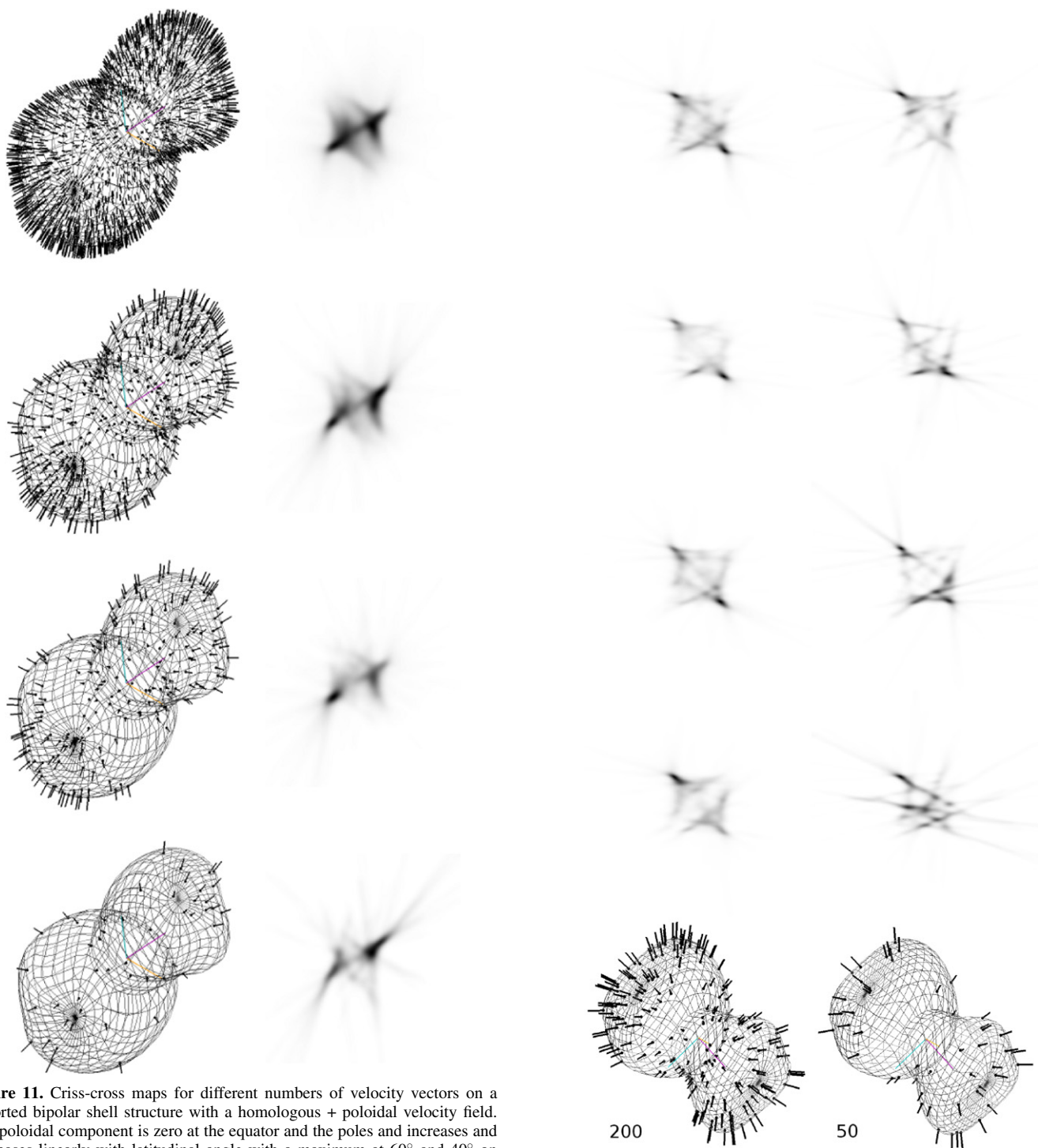


**Figure 11.** Criss-cross maps for different numbers of velocity vectors on a distorted bipolar shell structure with a homologous + poloidal velocity field. The poloidal component is zero at the equator and the poles and increases and decreases linearly with latitudinal angle with a maximum at  $60^\circ$  and  $40^\circ$  on either side. From top to bottom, there are 2000, 500, 200, and 50 vectors in a map. We also include the 3D mesh with the particles and the projected vectors to illustrate the distributions.

(A color version of this figure is available in the online journal.)

field, the structure is lost and the criss-cross map basically fills out the area covered by the vectors.

### 3.3. Limitations and Potential Extensions

The main limitation of criss-cross mapping is ambiguity, i.e., there might always be several velocity fields combined within a given structure that produce the same result. Combining other types of data, such as spatially resolved spectroscopy, and using

**Figure 12.** Criss-cross maps for different random distributions of the sampling positions on an otherwise identical object for 200 and 50 vectors on the left and right, respectively. At the bottom, a representative distribution of vectors is shown for each vertical set.

(A color version of this figure is available in the online journal.)

symmetry considerations, may resolve these shortcomings. This mapping technique is therefore to be considered as a constraint and diagnostic tool that complements other methods in order to resolve ambiguities that those techniques might suffer.

The amount and quality of proper motion data obtainable for an object depends strongly on the nature of its projected distribution of emission. Best suited are those with sharp small-scale structures for which a magnitude and direction of motion

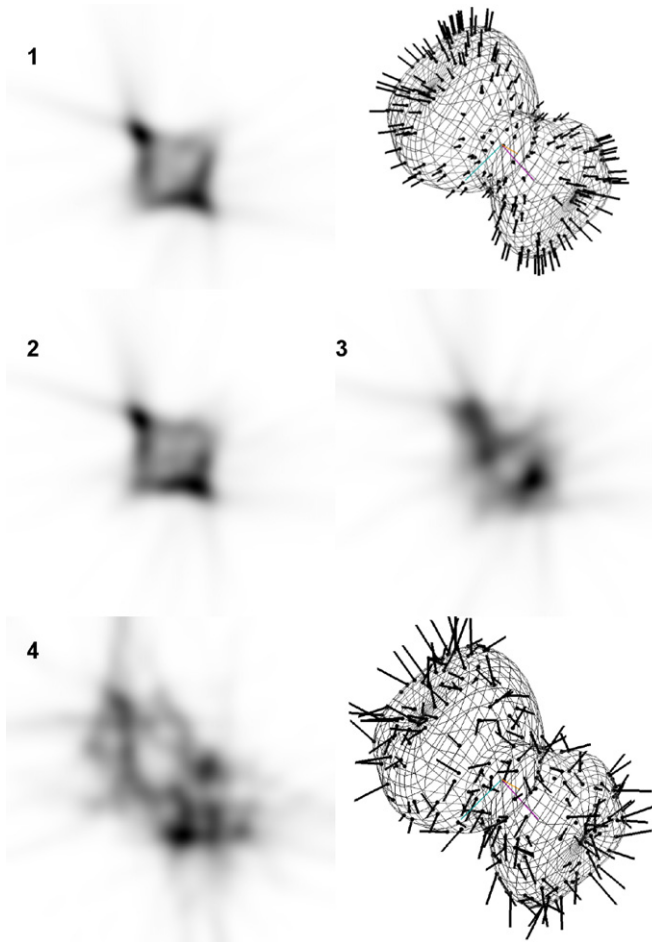


**Figure 13.** Influence of turbulence or measuring errors in a sequence of criss-cross maps. With a total of 200 vectors, we add an increasing random velocity component in Cartesian coordinates of equal average magnitude in each direction. The projected vectors are also shown for the first and last examples. (A color version of this figure is available in the online journal.)

can be measured with precision. Diffuse or very elongated structures without much substructure are less suitable. Further research of the general properties should reveal more limitations, as well as other potential benefits and applications.

Possible extensions of the method described here could be in a more differentiated use of the weighting of the individual lines. These could include information on the measuring errors, the velocity magnitude, the brightness in the image, or the radial velocity measured from spectroscopy. The brightness of the line could also vary with distance from the position of the vector, providing information about spatial correlation. The potential benefits from these types of extensions to the current basic scheme will be explored in a future paper.

#### 4. THE DIRECTION OF PROPER MOTION VECTORS IN BD+30 3639

Currently only very few objects have sufficient internal proper motion measurements to favorably apply criss-cross mapping. It is hoped that, future analysis of new and existing observations with criss-cross mapping in mind might yield new suitable data sets and new information about these objects. In this section, we apply the criss-cross mapping technique to BD+30 3639, with approximately 200 internal proper motion vectors published by LHB2002.

From Figures 3 and 4 of LHB2002, we determined the P.A.s and deviation  $\delta$  from the radial direction by direct measurement from the expanded image of the original paper using good old-fashioned ruler and protractor, since the numerical data were unavailable. The center for the angular measurement was in the middle of the central star image. We estimate the error in the measurement to be of the order of  $2^\circ$  in P.A. and  $\delta$ . The robustness of the criss-cross mapping procedure as shown in the previous section leads us to conclude that the results and conclusions for BD+30 3639 would not have changed if original numerical proper motion vector data had been available.

The distribution of  $\delta$  as a function of P.A. is plotted in Figure 2. We find that the distribution is not random around zero, as would be expected for a radial expansion with some random measurement errors. Instead, the deviation from radial direction follows approximately a sinusoidal pattern.

We have used the 3D morpho-kinematic modeling and reconstruction software *Shape* (Steffen et al. 2011; <http://www.astrosen.unam.mx/shape>) to reconstruct the 3D structure of BD+30 3639 based on the available imaging and internal proper motion from LHB2002 and  $P$ - $V$  diagrams from Bryce & Mellema (1999). For this initial reconstruction, we only used the  $[N \text{ II}]$  data as a reference, since they are expected to be more like a thin shell structure, rather than span a significant range in distance for every given direction from the central star. Working with thin shells reduces ambiguities in the reconstructions. A detailed morpho-kinematic model of BD+30 3639 based also on additional spectroscopic data will be published elsewhere (W. Steffen et al. 2011, in preparation).

The criss-cross mapping shows that the kinematic center is not located at the central star. Figure 1 (left) contains the criss-cross map superimposed on an observational composite image. There are well-defined peaks at approximately 0.5 arcsec from the central star. This map shows that the kinematic center of the expanding nebula is not located at the position of the central star. Figure 14 (right) is a model map which includes a 0.5 arcsec shift of the velocity field in the direction as deduced from the observed criss-cross map (Figure 14, middle). The structure is a simple elongated tri-axial ellipsoid aligned with the assumed direction of the molecular outflows. In addition to a homologous velocity component, there is a random noise in the velocity vector components of  $4 \text{ km s}^{-1}$  in each Cartesian direction, as well as a cylindrical velocity component of  $12 \text{ km s}^{-1}$  along the direction of the molecular outflows. The cylindrical component grows linearly from zero starting at half-way to the ends of the elongated ellipsoid, i.e., the cylindrical component is suppressed near the bright equatorial region. The detailed structure is not relevant. The structure and position of the model map is similar to the observed one, showing that the interpretation of an off-set kinematic center and a velocity disturbance due to the jets is a possible explanation for the observations. See Figure 2 for a comparison of the model and observations in terms of the directions of the vectors.

#### 5. DISCUSSION AND CONCLUSIONS

We have introduced a new technique, criss-cross mapping, for the analysis of the internal proper motion field measured in astrophysical nebulae. Criss-cross mapping was designed to easily detect deviations from radial expansion. Since a radial expansion produces a well-defined point-like structure at the projected position of the center of expansion, deviations from such an expansion produce characteristic patterns that can help

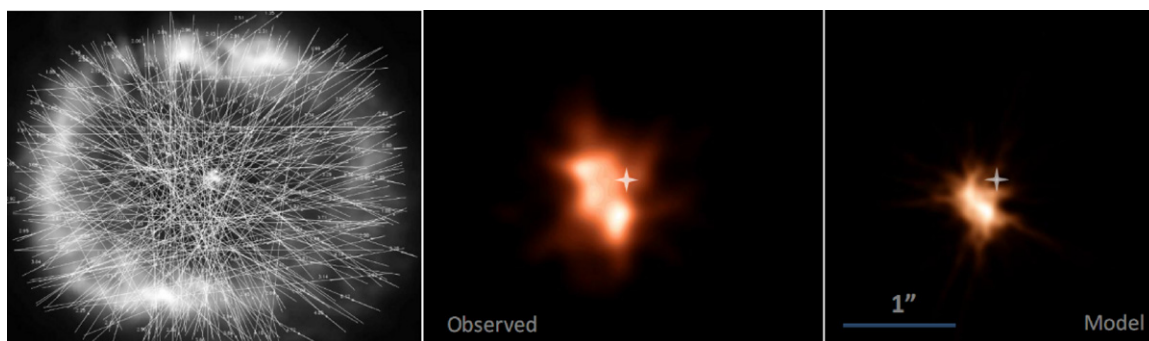


**Figure 14.** Straight lines overlaid on all proper motion vectors of Figure 3 from LHB2002 (left). The resulting line image has then been convolved with a Gaussian kernel to produce the criss-cross map in the middle, which is also shown in red in Figure 1 of this work. On the right is the corresponding criss-cross map from our *Shape* model.

(A color version of this figure is available in the online journal.)

to interpret the data and find effects that otherwise might have gone undetected.

We have identified some limitations of the method. The maps cannot be uniquely attributed to a particular velocity field. There may however be extensions to the current scheme that might improve this situation. Applying additional information to the weighting of the criss-cross lines will be investigated as a potential extension of the current method. Used as an additional constraint in modeling along with images and spatially resolved spectroscopy, criss-cross mapping can provide important additional information about the velocity field in an object.

Velocity vector data coverage on an object is important for the quality of a map, although the number of vectors needed for the key patterns to emerge is quite low. For this basic version of criss-cross mapping to work, only the direction of proper motion is needed. Special care should be given to the determination of the direction, not only to the magnitude. To our knowledge, the best current measurement of the internal proper motion vectors of PNe is for BD+30 3639. We have therefore used these measurements by LHB2002 as the first application of criss-cross mapping.

The application to BD+30 3639 leads us to conclude that the kinematic center is offset from the central star. The lines connecting the molecular outflow with the central star and the peaks of the criss-cross map suggest that the tails of the outflows might be directed toward the newly deduced kinematic center (Figure 1). This conclusion does require confirmation, since the elliptical beam of the molecular map is approximately aligned with the direction between the southern outflow and the peak and structure of the criss-cross map. This problem does not, however, occur for the northern component, which shows a similar alignment with the criss-cross structure.

Reasons for the offset of the kinematic center could be motion of the central star within the nebula. There is, however, no evidence for that, since the star appears to be well centered on

the optical image of the nebula. Another option is the presence of a secondary object that is responsible for the ejection of the bipolar molecular outflow. The distance of the object would be 600 AU or more from the central star. The molecular outflow might have distorted the velocity field producing the observed offset and deviations from a homologous expansion.

This work has been supported by grants from CONACYT 49447 and UNAM PAPIIT IN100410. N.K. received additional support from the Natural Sciences and Engineering Council of Canada (NSERC) and from the Killam Trusts.

## REFERENCES

- Bachiller, R., Forveille, T., Huggins, P. J., Cox, P., & Maillard, J. P. 2000, *A&A*, **353**, L5
- Balick, B., & Frank, A. 2002, *ARA&A*, **40**, 439
- Bryce, M., Balick, B., & Meaburn, J. 1994, *MNRAS*, **266**, 721
- Bryce, M., & Mellema, G. 1999, *MNRAS*, **309**, 731
- Guerrero, M. A., Manchado, A., & Chu, Y.-H. 1997, *ApJ*, **487**, 328
- Harrington, P., Lame, N. J., White, S., & Borkowski, K. 1997, *AJ*, **113**, 2147
- Kastner, J. H., Soker, N., Vrtilik, S. D., & Dgani, R. 2000, *ApJ*, **545**, L57
- Li, J., Harrington, J. P., & Borkowski, K. 2002, *AJ*, **123**, 2676
- Meaburn, J., Lloyd, M., Vaytet, N. M. H., & López, J. A. 2008, *MNRAS*, **385**, 269
- Mellema, G. 2004, *A&A*, **416**, 623
- O'Dell, C. R., Henney, W. J., & Sabbadin, F. 2009, *AJ*, **137**, 3815
- Schönberner, D., Jacob, R., & Steffen, M. 2005, *A&A*, **441**, 573
- Shupe, D. L., Larkin, J. E., Knop, R. A., Armus, L., Matthews, K., & Soifer, B. T. 1998, *ApJ*, **498**, 267
- Steffen, W., García-Segura, G., & Koning, N. 2009, *ApJ*, **691**, 696
- Steffen, W., Koning, N., Wenger, S., Morisset, C., & Magnor, M. 2011, *Shape: A 3-D Modeling Tool for Astrophysics*, IEEE Trans. on Visualization & Computer Graphics, in press (arXiv:1003.2012)
- Steffen, W., & López, J. A. 2004, *ApJ*, **612**, 319
- Steffen, W., López, J. A., Koning, N., Kwok, S., Riesgo, H., Richer, M. G., & Morisset, C. 2007, in *Asymmetrical Planetary Nebulae IV*, ed. R. L. M. Corradi, A. Manchado, & N. Soker, La Palma, 2007 June 18–22, Published online at <http://www.iac.es/project/apn4>, article 38